Optical and Quantum Electronics (2020) 52:467
https://doi.org/10.1007/s11082-020-02580-6

Negative refraction in the double quantum dot system

Hussein G. Al-Toki[1] · **Amin Habbeb Al-Khursan**[1]

Received: 8 July 2020 / Accepted: 3 October 2020

Abstract
This work proposes a double quantum dot (DQD) system, with a wetting layer (WL) is included, to study the negative refractive index (NRI) under the application of the electric fields: pump, probe, and fields between WL-QD state, in addition to the magnetic field. The density matrix theory is used to write the equation of motion and an orthogonalized plane wave is used between WL-QD states. The results show that the DQD system exhibit NRI ordinarily until with pump and probe signals, only, due to the manipulation between states. A high NRI corresponding to neglected absorption is obtained under applied electric fields between QD-QD, the conduction (CB) and valence bands (VB) WL-QD fields. It is shown that the main requirement in increasing NRI is the high electric gain connected with a low magnetic one. This can be obtained under five applied electric fields in addition to a high VB WL-QD electric field. Neglecting WL reduces NRI by ~ 16 times. In single QD, the NRI is very small compared with DQD.

Keywords Negative refractive index · Double quantum dot · Wetting layer-quantum dot transition

1 Introduction

The direct products of reaction with the electromagnetic wave are represented by two secondary recurrence information: the electrical permittivity (ε) and the magnetic permeability (μ). It has been shown that material with both ε and $\mu < 0$ will provide a negative refractive index (NRI). It is also critical that there would be overlapping negative permittivity and permeability values across a large range of detuning (Shelby et al. 2001; Padilla et al. 2006). In research published in 1968, Veselago predicted that electromagnetic plane waves in a medium possessing at the same time negative permeability and permittivity will propagate in the reverse direction to the one of electricity transfer (Veselago and Narimanov 2006; Veselago 1968; Smith et al. 2000). These negative refraction materials promise several applications, for example, the negative Goos-Hanchen shift enhancement of the evanescent wave (Berman 2002), enhancement of transitory waves, and centering

✉ Amin Habbeb Al-Khursan
ameen_2all@yahoo.com

[1] Nasiriya Nanotechnology Research Laboratory (NNRL), Science College, Thi-Qar University, Nasiriya, Iraq

of subwavelength (Fang et al. 2016). More surprisingly, it might be necessary to build a "perfect lens" in which the diffraction maximum is not restricted by the usage of a negative refractive material slab. The ideal lens has a picture quality that does not subject to limitations of the normal wavelength diffraction range (Veselago et al. 2006).

There have been several solutions to the development of NRI which are restricted to the artificial structures, such as metamaterials, photonic crystals, chiral products, and resonant photonic media. Negative refraction also results in resonant absorption particularly at higher frequencies, which restricts several potential applications (Lukin et al. 1999; Zhao et al. 2012). Involving a variety of electrical and magnetic periodic resonators produce serious difficulties in the manufacture of such optical systems (Drachev et al. 2006; Dolling et al. 2007).

E. Verhagen et al. achieving NRI in coupled plasmonic waveguides at optical frequencies (Verhagen et al. 2010). S. Foteinopoulou et al. examining NRI for an electromagnetic wave at a positive–negative interface of the refractive index in a photonic crystal (Foteinopoulou et al. 2003). NRI is obtained without negative permeability requirement by the electromagnetically induced charity that results from coherently coupling magnetic and electric dipole transitions (Kastel et al. 2007).

The possibility of attaining NRI in the photonic media by modifying the permeability is examined in a three-level atomic medium first. This brought the researches into dealing with solid-state systems. The obstacle facing this task is to find a system with two levels separated by the optical frequency with a nonvanishing matrix element of the magnetic dipole moment. Since QDs are completely quantized nanocrystals with size-controllable energy states, it is adequate to engineering QDs under an external electric field (Zhao et al. 2012; Al-Ameri et al. 2019).

H. Wang and K. Zhu tuning the refractive index of quantum dots (QDs) between negative and positive by changing their tunneling rate (Wang and Zhu 2010). The negative refractive index can be obtained under the application of a pulsed laser and bias voltage by changing the tunneling intensity between states of the quantum dot (QD) system. With rising a bias voltage, the refractive index may be changed to zero at the same time with zero permittivity and permeability. If the variable pulsed laser is applied to the QD device, it is also possible to achieve the NRI with very little damage (Pendry 2000).

To gain more controllability of characteristics, a double QD system is predicted (Villas-Bôaset al. 2004; Borges et al. 2012). In this sense, a Y-configuration double QD (DQD) system is proposed (Al-Nashy et al. 2014). Then, the ladder-plus-Y-DQD system including the wetting layer (WL) with an orthogonalized plane wave is considered to simulate the real QD structure (Abdullah et al. 2015). The optical characteristics are improved in this structure (Al-Nashy et al. 2018; Rehman and Al-Khursan 2016).

It is known that for material with weak effective Lande g factor, the spin–orbit coupling in the self-assembled DQD is neglected (Miladic et al. 2020). For materials with high Lande factor such as InSb nanowire, the spin–orbit coupling is very strong (Stavrou 2018). There is another type of DQDs, it is the gated DQDs where the QDs are connected via a gate (Wang et al. 2011). This type also contains an isolated DQDs which can be controlled via a gate, also (Gorman et al. 2005). InAs/GaAs DQDs is the best example of self-assembled DQD type, the case of study in this work. While the interdot distance is of crucial importance in the spin-flip mechanisms (Stavrou 2018), here, the carrier relaxation with the electric-dipole coupling is dominant.

In this work, NRI in the double quantum dot (DQD) system is proposed considering both conduction (CB) and valence bands (VB) in the field application, in addition to the wetting layer (WL). Electric fields: the pump Ω_{31} and the probe Ω_{20} and the magnetic field (Ω_{23}^{m}) are applied. These fields are applied between QD states as referred from their

subscript numbers, see Fig. 1. Additionally, other electric fields are applied between WL-QD states. During this theoretical work, the density matrix theory is used to write the equation of motion of this system. Using the quantum disk model, the energy states of the QDs are calculated. Orthogonalized plane wave (OPW) is used between WL and QD states, the momenta of different transitions are calculated through this process as offered by our Matlab software built in our laboratory. The following types of electric components from the optical fields are examined: QD-QD which are the pump and the probe, CB WL-QD, and VB WL-QD, this type of field is not examined earlier. Also, the effect of the WL continuum state, and the results are compared with the single QD case. Increasing NRI requires a high electric gain connected with a low magnetic one. This can be obtained under five applied electric fields with a high VB WL-QD electric field which is of important effect.

2 Density matrix equations of the DQD system

For the DQD system shown in Fig. 1, its Hamiltonian can be represented by,

$$i\hbar\dot{\rho} = [\mathrm{H}_0, \rho] + [\mathrm{H}_{in}, \rho] + [\mathrm{H}_{relex}, \rho] \tag{1}$$

ρ is the density matrix operator and $\dot{\rho} = (d\rho/dt)$ $\mathrm{H}_0, \mathrm{H}_{in}$, H_{relex} are the unperturbed, the interaction, and the relaxation Hamiltonians. The unperturbed Hamiltonian H_0 is diagonal in $|i\rangle$, $(i = 0, 1, 2, 3, 4)$ states and results in $\hbar w_i$ energy which is the central transition energy, i.e.

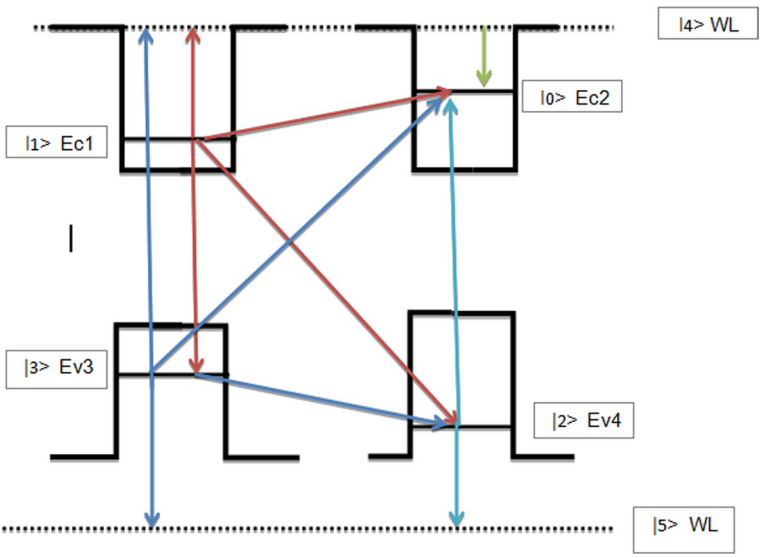

Fig. 1 Energy band illustration for the DQD system with WL. (Color figure online)

$$H_0 = \hbar w_0|0\rangle\langle 0| + \hbar w_1|1\rangle\langle 1| + \hbar w_2|2\rangle\langle 2| + \hbar w_3|3\rangle\langle 3| + \hbar w_4|4\rangle\langle 4| + \hbar w_5|5\rangle\langle 5| \quad (2)$$

In Eq. (1), H_{relex} is the relaxation Hamilton that takes into account the relaxations resulting from the processes of scattering. They are represented by the relaxation rates. The interaction Hamiltonian for this DQD system is written as

$$H_{\text{int}} = \begin{bmatrix} 0 & -\hbar A_{01} & -\hbar\Omega_{02} & -\hbar\Omega_{03} & -\hbar\Omega_{04} & 0 \\ -\hbar A_{01} & 0 & -\hbar T_{12} & -\hbar\Omega_{13} & -\hbar\Omega_{14} & 0 \\ -\hbar\Omega_{02} & -\hbar T_{12} & 0 & -\hbar\Omega^m_{23} & 0 & -\hbar\Omega_{25} \\ -\hbar\Omega_{03} & -\hbar\Omega_{13} & -\hbar\Omega^m_{23} & 0 & 0 & -\hbar\Omega_{35} \\ -\hbar\Omega_{04} & -\hbar\Omega_{14} & 0 & 0 & 0 & 0 \\ 0 & 0 & -\hbar\Omega_{52} & -\hbar\Omega_{53} & 0 & 0 \end{bmatrix} \quad (3)$$

where Ω^m_{23} is the magnetic Rabi frequencies of the atomic transitions between $|2\rangle \leftrightarrow |3\rangle$ states, Ω_{ij} is the Rabi frequency of the electric field component of the optical field applied between $|i\rangle$ and $|j\rangle$ states, T_{12} is the tunneling component, $A_{ij} = \mu^2_{ij}\omega^2_{ij}/A$ with $A = 3\pi\hbar\varepsilon_0 c^3$, and c is the speed of light. Depending on the above Hamiltonian and under the rotating wave approximation, the density matrix equations for the DQD system shown in Fig. 1 are written in Eq. 36 in the "Appendix".

3 DQD structure

The QD molecule used here is composed of two QDs separated by barrier material of few nanometers. It is well known that when the separation between QDs is > 9 nm the excitonic picture is dominant in the carrier description. Because of this nanoscale separation, the electrons are delocalized from the electron states. The transition between states can be strengthened by different effects such as tunneling or applied fields (Veselago et al. 2006). Such a QD molecule is fabricated by a self-assembled growth technique. A realistic structure of DQDs is detected in InAs/GaAs (Tarasov et al. 2006) and used in many works, like (Mahmoudi and Sahrai 2009).

The DQD considered is composed of two QDs, each QD was an InAs QD with a disk shape of the radius of a and height of h. The sizes of the first QD are ($h = 2$ nm, $a = 14$ nm) while those of the second QD are ($h = 3.5$ nm, $a = 13$ nm). Each QD has one conduction and valence subbands. The WL (InGaAs quantum well layer with 2 nm thickness) conduction and valence subbands are the reservoir states for both QDs. The structure is grown on a GaAs barrier. The used parameters for calculations are covered from (Kim and Chuang 2006; Chuang 2009). The calculated QD conduction subbands are 791.5 meV for state $|0\rangle$ and 796.2 meV for the state $|1\rangle$ while the corresponding valence subbands are 331.1 meV for state $|2\rangle$ and 331.5 for the state $|3\rangle$. A sketch of the energy band diagram for the DQD structure was shown in Fig. 1. The work is done under MATLAB by using our code (MAOUD-37) that is written in our laboratory to simulate QD problems beginning from QD energy subband calculation, going to QD optical properties. This code is checked with experiment (Al-Husseini et al. 2009) and used in a large number of our published papers such as (Al-Ameri et al. 2019; Al-Nashy et al. 2014; Abdullah et al. 2015; Al-Nashy et al. 2018; Rehman et al. 2016; Al-Salihi and Al-Khursan 2020).

4 Negative refractive index

The QD electrical susceptibility, α_e, associated with the electrical field of the probe is given by,

$$\alpha_e = (\frac{\mu_{02}\rho_{02}}{\varepsilon_\circ \mathrm{E}_{02}}) \tag{4}$$

where $\varepsilon_\circ$ is the permittivity of free space, μ_{02} is the electronic dipole moments of the respective transformation, ρ_{02} is the corresponding density operators, finally, E_{02} is the corresponding optical coupling field. The permittivity is given by (Fang et al. 2016),

$$\varepsilon = \varepsilon_r + i\varepsilon_i = \frac{1 + \frac{2}{3}N_Q\alpha_e}{1 - \frac{1}{3}N_Q\alpha_e} \tag{5}$$

where $\mathrm{N_Q}$ is the QD density, ε_r and ε_i are the real and the imaginary parts of the permittivity, respectively. For the magnetic susceptibility α_m of the QD,

$$\alpha_m = \frac{\mu_{23}^m}{B_{23}\rho_{23}} \tag{6}$$

where μ_{23}^m is the magnetic transition momentum between $|2\rangle \leftrightarrow |3\rangle$ states. In this work, the magnetic moment μ_{23}^m is taken equal to the Boher magneton μ_B, ρ_{23} is the density operator, and B_{23} is the magnetic flux density. The magnetic spontaneous emission rate is defined by (Shelby et al. 2001),

$$\alpha_m = \mu_0 \frac{{\mu_{23}}^m}{B_{23}}\rho_{23} \tag{7}$$

Where μ_0 is the vacuum permeability and μ_{23}^m is the magnetic transition. The permeability is given by (Veselago et al. 2006),

$$\mu = \mu_r + i\mu_i = \frac{1 + \frac{2}{3}N_Q\alpha_m}{1 - \frac{1}{3}N_Q\alpha_m} \tag{8}$$

μ_r and μ_i is the real and imaginary parts, respectively, of permeability. To see the impact of the field area, the following expressions of μ_r and μ_i are obtained (Fang et al. 2016),

$$\mu_r = \frac{1 + \frac{1}{3}\mathrm{Re}[N_Q\alpha_m] - \frac{2}{9}|N_Q\alpha_m|^2}{1 - \frac{1}{3}\mathrm{Re}[N_Q\alpha_m]^2 + (\frac{1}{3}\mathrm{Im}[N_Q\alpha_m])^2} \tag{9}$$

and

$$\mu_i = \frac{\mathrm{Im}[N_Q\alpha_m]}{1 - \frac{1}{3}\mathrm{Re}[N_Q\alpha_m]^2 + (\frac{1}{3}\mathrm{Im}[N_Q\alpha_m])^2} \tag{10}$$

$\mathrm{Re}[N\alpha_m] < 0$ and > 1 is needed for the realization of negative μ_r for a moderate atomic density value. The negative real part of magnetic susceptibility can be understood with appropriate phases by initial atomic coherence. For specifically related permittivity and

permeability; negative refraction $n = -\sqrt{\varepsilon_r}\mu_r$ is obtained when $\varepsilon_r < 0$ and $\mu_r < 0$ (Shelby et al. 2001). The real (n_r) and imaginary (n_i) parts of the refractive index are represented in the case of complex-valued ε and μ_r by (Fang et al. 2016),

$$n_r = -\frac{1}{\sqrt{2}}\sqrt{|\varepsilon||\mu| + \mu_r\varepsilon_r - \mu_i\varepsilon_i} \tag{11}$$

and

$$n_i = -\frac{1}{\sqrt{2}}\frac{\mu_i\varepsilon_r + \mu_r\varepsilon_i}{\sqrt{|\varepsilon||\mu| + \mu_r\varepsilon_r - \mu_i\varepsilon_i}} \tag{12}$$

Size fluctuations in the self-assembled QD structure are inevitable. It can be taken by adjusting the definition of the susceptibility (α_e, α_m) to considering the Gaussian (inhomogenous) distribution of the QD ensemble. Of course, this introduces some changes but, the main conclusions drawn for this work remain the same and the results here represent an average of a single group of QDs (Al-Khursan et al. 2009, 2012).

5 Wavefunctions and orthogonalized plane wave

To obtain the energy subbands, the Schrodinger equation $H\psi = E\psi$ is solved for the quantum disk in the cylindrical coordinates where it is written as,

$$-\frac{\hbar^2}{2m^*}\left[\frac{1}{\rho}\frac{\partial}{\partial\rho}\left(\frac{1}{\rho}\frac{\partial}{\partial\rho}\right) + \frac{1}{\rho^2}\frac{\partial^2}{\partial\phi^2} + \frac{\partial^2}{\partial z^2}\right]\psi(\rho,\phi,z) + V\,\psi(\rho,\phi,z) = E\,\psi(\rho,\phi,z) \tag{13}$$

The solution can be considered under the separation of variables into in-plane ($\rho - \phi$) direction and the z-direction. In the in-plane direction, the solution is assumed in the form,

$$\Psi(\rho,\phi) = \frac{e^{im\phi}}{\sqrt{2\pi}}\begin{cases}\phi_{QD}(\vec{\rho}) & \rho \le a \\ C_2 K_m(q\rho) & \rho > a\end{cases} \tag{14}$$

where $K_m(q\rho)$ is the 2$^{\text{nd}}$ order Bessel function with

$$q = \frac{\sqrt{2m_b^*(V_b - E_\rho)}}{\hbar} \tag{15}$$

m_b^*, V_b are, respectively, the effective mass and the potential in the WL, while E_ρ is the QD energy in the in-plane direction.

The in-plane QD wavefunction is represented by the first kind of the Bessel function, $J_m\left(p\vec{\rho}\right)$ (Kim and Chuang 2006),

$$\phi_{QD}\left(\vec{\rho}\right) = C_{nm}J_m\left(p\vec{\rho}\right) \tag{16}$$

where C_{nm} is the normalization constant, p is a constant defined by

$$p = \frac{\sqrt{2m_d^*(E_\rho - V_d)}}{\hbar} \tag{17}$$

m_d^*, V_d are, respectively, the effective mass and the potential of the QD in the in-plane direction. V_d is taken zero inside the disk.

By considering the boundary conditions (BCs) for the wavefunction and its first-order derivative between the QDs and the WL, the quantized constants p (in Eq. 18) and q (in Eq. 16) can be calculated and the in-plane energy is then obtained as (Kim and Chuang 2006)

$$E_\rho = \frac{\hbar^2}{2m_d^*}\frac{(pa)^2}{a^2} \tag{18}$$

In the z-direction, the QD wavefunction is similar to that of the quantum well and is defined as,

$$\Psi(z_\sigma) = \begin{cases} A_{z_\sigma}\cos(k_{z_\sigma} z) & z \le h/2 \\ C_3 \exp\{\frac{\sqrt{2m_b^*(\Delta E_c - E_{z_\sigma})}}{\hbar}} & z > h/2 \end{cases} \tag{19}$$

For the height h of the QD (or the thickness of the WL), $\sigma = QD$ for QD wavefunction while $\sigma = WL$ for WL wavefunction. A_{z_σ} is their normalization constants and ΔE_c is the band edge discontinuity for the conduction band (the subscript c is replaced by v in the case of valence band). E_{z_σ} is the subband of the QD in the z-directions (or for the WL in the case of WL wavefunction). Then, the entire QD wavefunction is defined as (Al-Ameri et al. 2019),

$$\varphi_{QD}(\vec{r}) = \varphi_{QD}(\vec{\rho}) A_{Z_{QD}} \cos\left(k_z z\right) u(\vec{r}) \tag{20}$$

$u(\vec{r})$ is the periodical Bloch function. Applying the BCs, the QD eigen energy in the z-direction is obtained by the relation (Kim and Chuang 2006),

$$E_z = \frac{\hbar^2}{2m_d^*}\frac{(k_z h/2)^2}{(h/2)^2} \tag{21}$$

Then, the total eigen energy of the disk is $E_d = E_\rho + E_z$.

The wavefunction in the WL is represented by a plane wave multiplied by the confined state wavefunction in the perpendicular (z) direction. So, the transition is impossible between the QD states and the unquantized part of the WL which is the in-plane (x–y disk plane) part of the WL wavefunction, i.e. there is orthogonality between the QD wavefunctions in the disk-plane and the in-plane WL wavefunction.

An orthogonalized plane wave (OPW) is defined in the in-plane direction in the WL. It is composed of the WL and the in-plane QD wavefunctions, and is defined as follows (Al-Ameri et al. 2019),

$$|\psi_{WL}\rangle = \frac{1}{N_{WL}}\left[|\varphi_{WL}\rangle - \sum_{\ell} \left|\varphi_{QD}^{\ell}\right\rangle \left\langle \varphi_{QD}^{\ell} \middle| \varphi_{WL}\right\rangle\right] \tag{22}$$

where the subscript ℓ refers to the QD state in the in-plane direction. $\varphi_{WL}(\vec{\rho})$ is the WL (quantum well) in-plane wavefunction which is written as (Asada et al. 1984),

$$\varphi_{WL}(\vec{\rho}) = A_{W\rho} \exp\left(i\vec{k}_{w\rho} \cdot \vec{\rho}\right) \tag{23}$$

$\vec{k}_{w\rho}$ is the wavevector in the in-plane WL, A_{W_ρ} is the in-plane WL normalization constant. The normalization constant in the OPW in Eq. (23) is defined by (Rehman and Al-Khursan 2016),

$$N_{WL} = \sqrt{1 - \left| \sum_i \left\langle \varphi^i_{QD} \mid \varphi_{WL} \right\rangle \right|^2} \tag{24}$$

The summation runs over all the DQD subbands.

6 WL-QD momentum matrix elements

For the WL-QD transition, the momentum matrix element is defined here with an assignment for the band that the state in it. For example, μ_{35}, is the momentum for the WL-QD transition in the VB. It is given by,

$$\mu_{35} = \left\langle \phi^{j=3}_{QD} \middle| er \middle| \phi_{WL_v} \right\rangle \tag{25}$$

with

$$\mu_{35} = \left\langle \varphi^{j=3}_{QD} \middle| e\hat{\rho}\rho \middle| \psi_{WL_v} \right\rangle A_{QD_{z_3}} A_{W_{z_5}} \int \cos(k_{z_v} z)\, \cos(k_{zw_v} z) dz \tag{26}$$

$$\left\langle \phi^{j=3}_{QD} \middle| e\hat{\rho}\rho \middle| \psi_{WL_v} \right\rangle = \frac{1}{\mathrm{N}_{WL}} \left[\left\langle \varphi^{j=3}_{QD} \middle| e\rho \middle| \varphi_{WL_v} \right\rangle - \sum_{i=0}^{3} \left\langle \varphi^{j=3}_{QD} \middle| e\rho \middle| \varphi^i_{QD} \right\rangle \left\langle \varphi^i_{QD} \middle| \varphi_{WL_v} \right\rangle \right] \tag{27}$$

$$\left\langle \varphi^{j=3}_{QD} | e\rho | \varphi_{WL_v} \right\rangle = \frac{C_{mn}|e|}{\sqrt{\mathrm{A}}} \int J_{m,j}(p\rho)\, e^{ik\rho} \rho^2 d\rho \tag{28}$$

$$\left\langle \varphi^{j=3}_{QD} \middle| e\rho \middle| \varphi^{i=2}_{QD} \right\rangle = C_{mn,j} C_{mn,i} |e| \int_0^{h/2} J_{m,j} \rho J_{m,i} \rho d\rho \tag{29}$$

$$\left\langle \varphi^{i=2}_{QD} \middle| \varphi_{WL_v} \right\rangle = \frac{C_{nm}}{\sqrt{A}} \int J_{m,j}(p\rho)\, e^{ik\rho} \rho^2 d\rho \tag{30}$$

Then, taking μ_{14} as an example of the WL-QD transition in the CB. It is defined as follows,

$$\mu_{14} = \left\langle \phi^{j=1}_{QD} \middle| er \middle| \phi_{WL} \right\rangle \tag{31}$$

$$\mu_{14} = \left\langle \varphi^{j=1}_{QD} \middle| e\hat{\rho}\rho \middle| \psi_{WL} \right\rangle A_{QD_{z_1}} A_{W_{z_4}} \int \cos(k_z z)\, \cos(k_{zw} z) dz \tag{32}$$

$$\left\langle \phi_{QD}^{j=1} \middle| e\hat{\rho}\rho \middle| \psi_{WL} \right\rangle = \frac{1}{\mathrm{N}_{WL}} \left[\left\langle \varphi_{QD}^{j=1} | e\rho | \varphi_{WL} \right\rangle - \sum_{i=0}^{1} \left\langle \varphi_{QD}^{j=1} | e\rho | \varphi_{QD}^{i=0} \right\rangle \left\langle \varphi_{QD}^{i=0} | \varphi_{WL} \right\rangle \right] \quad (33)$$

$$\left\langle \varphi_{QD}^{j=1} \middle| e\rho \middle| \varphi_{QD}^{i} \right\rangle = C_{mn,j} C_{mn,i} |e| \int_{0}^{h/2} J_{m,j} \rho J_{m,i} \rho \; d\rho \quad (34)$$

$$\left\langle \varphi_{QD}^{i=0} | \varphi_{WL} \right\rangle = \frac{C_{nm}}{\sqrt{A}} \int_{0}^{a} J_m(\rho\vec{\rho})\, e^{ik\rho} \rho \; d\rho \quad (35)$$

7 Results and discussion

While the input signals are introduced in this work by their Rabi frequencies, it is possible to calculate their powers (p_s) from the relation of the squared electric amplitude $|E_s|^2 = (p_s / c\varepsilon_0 WD)$ where W and D are the thickness and width of the active region (Kim et al. 2008). The power relation is related to the active region thickness which can be the same for different structures (external sizes) while the Rabi frequency is related to the energy between states, considering detuning. Thus, Rabi frequency is more feasible to describe applied fields as used in a wide area of optical applications in an unlimited number of papers. Throughout all the results, the QD density used in the calculations is $\mathrm{N}_Q = 1.4 \times 10^{17}\, cm^{-3}$, $\gamma_0 = 0.4 GHz$ (Ben-Ezra et al. 2005), and the tunneling component is taken $T_{12} = 8\gamma_0$. The absorptions $\mathrm{Im}(\alpha_e, \alpha_m)$ are unit less since they are multiplied by N_Q. The peak wavelength is 1101.8 nm which is the wavelength between $|0\rangle$ and $|2\rangle$ states (states of the probe field). Although this structure can work at zero bias (small or neglected tunneling), the tunneling in this DQD structure between the two QDs may be attained by applying an external bias to the gate electrodes (Asadpour et al. 2011). More explanation about the relation between tunneling and the applied voltage can be seen in (Sahrai et al. 2014).

Figure 2 shows the electric and magnetic susceptibilities under two electric (Ω_{20}, Ω_{31}) and magnetic (Ω_{23}^m) fields. Their absorptions $\mathrm{Im}(\alpha_e, \alpha_m)$ have small values as in Fig. 2-2 and 2-4. The electric susceptibility is a result of the interaction of four levels while the magnetic susceptibility is due to the interaction of a two-level system. The quantum interference between these states results in negative refraction. Although of this, increasing the absorption shown in Fig. 2-2 prevents negative refraction from more increment. Figures 2-5 to 2-8 shows the real and imaginary parts of electric (ε) and magnetic μ permeability. They show that the local field effect is dominated by a curved behavior but not zero at the central probe field detuning for both them. From both permittivity and permeability results (Figs. 2-5 to 2-8), it is shown that the DQD system is passive for permittivity at the high energy side of detuning ($\Delta_{20} = 0 - 100\gamma$), while it is passive for permeability at the low energy side of detuning ($\Delta_{20} = -300 - 50\gamma$). Accordingly, a negative refractive index is obtained at a large range of detuning in Fig. 2-9. In this figure, a dip is shown near zero-detuning with two dissimilar side peaks appear at $\Delta_{20} = 150\gamma$. This NRI is exerted along with all the detuning range by a small value of magnetic susceptibility. In Fig. 2 and all of

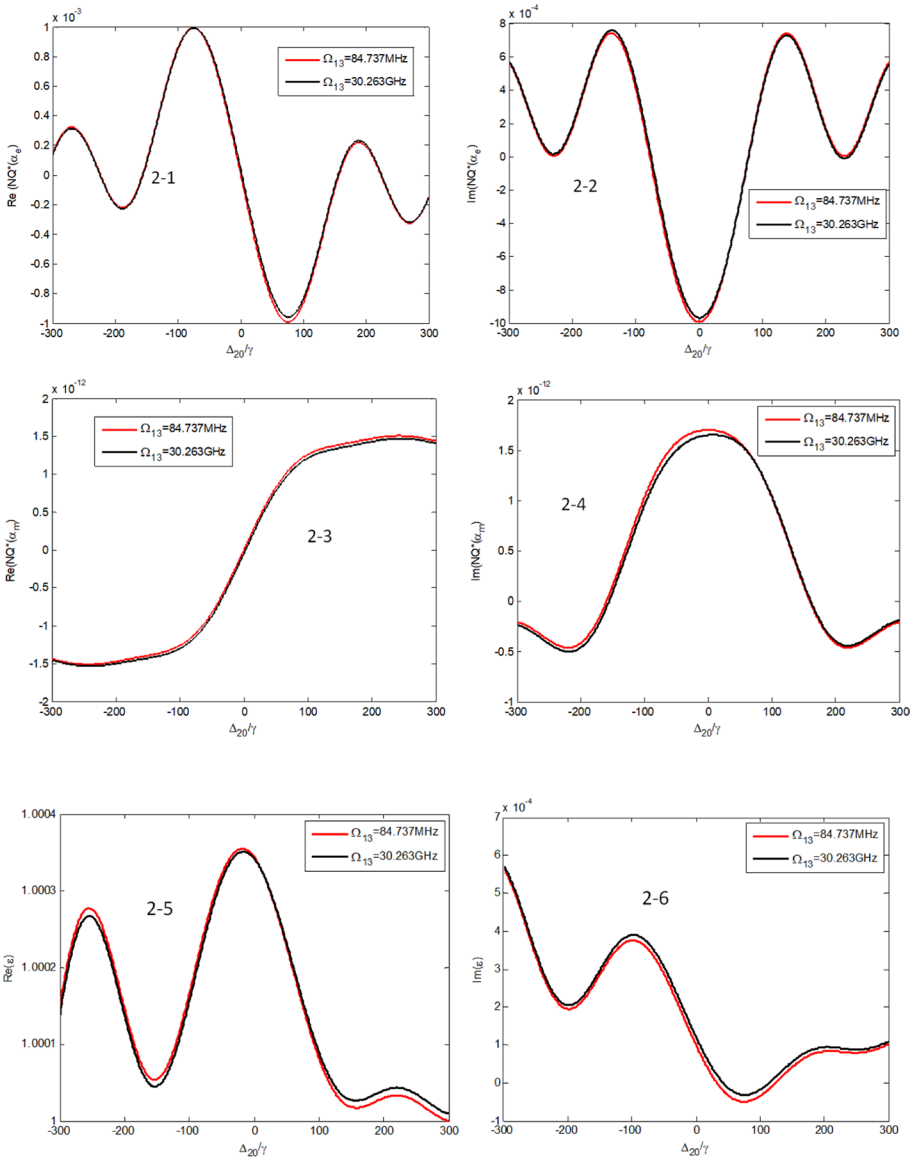

Fig. 2 Real and imaginary parts of: 2-1, 2-2 electric and 2-3, 2-4 magnetic susceptibility, 2-5, 2-6 electric 2-7, 2-8 and magnetic permeability, and 2-9, 2-10 refractive index at weak probe electric field $\Omega_{20} = 14.567 MHz$. (Color figure online)

the figures (thereafter), the range of detuning is so wide which is also shown in the work of (Kastel et al. 2007).

Figure 3 shows the same set of figures under the application of four optical fields in addition to the magnetic field. Here, in addition to the pump and probe (Ω_{20}, Ω_{13}), there are two fields from the type CB WL-QD and VB WL-QD (Ω_{04}, Ω_{35}), respectively. The effect of adding these two fields gives good discrimination between the two curves when

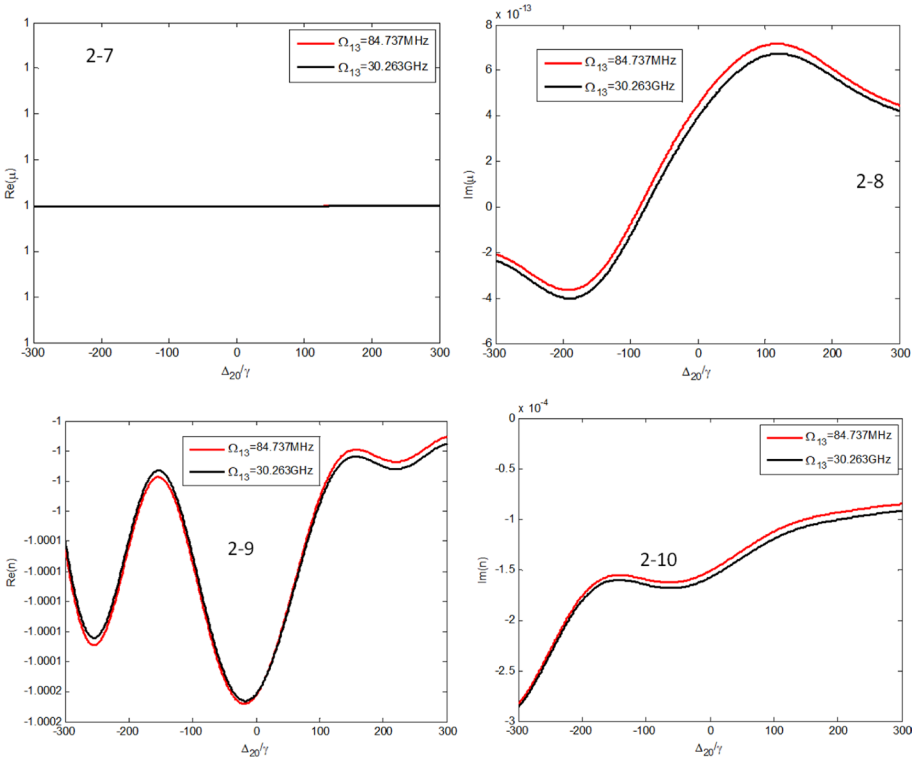

Fig. 2 (continued)

the field Ω_{31} is increasing. The real parts of permittivity (ε) and permeability (μ) are > 0. Mainly, the values obtained are in the same range and then, the NRI is not so increasing. The quantum interference is created under the application of CB WL-QD and VB WL-QD (Ω_{04}, Ω_{35}) electric fields as shown in the red curve in Fig. 3-2 where an EIT window is shown and NRI is increasing as in the red curve in Fig. 3-9. This means that the two WL-QD fields are taking the carriers to other states, couples the DQD states due to EIT occurrence. This type of quantum interference is examined in the ladder-plus-Y DQD system (Al-Ameri et al. 2019). With increasing Ω_{31} field, the gain (negative part of Im(α_e), red curve) in Fig. 3-2 changes to absorption (positive part of Im(α_e), black curve), and NRI is reduced as in Fig. 3-9. The EIT window is removed and the absorption is peaked with increasing Ω_{31}, as in the black curve in Fig. 3-2, which reduces the NRI, as in the black curve in Fig. 3-9.

Figure 4 shows the effect of applying four electric fields Ω_{20}, Ω_{31}, Ω_{04}, Ω_{25} and the magnetic field (Ω_{23}^{m}). Here, the difference from Fig. 3 is a reduced Ω_{04} field with a higher VB WL-QD optical field Ω_{25} is taken instead of the Ω_{35} field. This shows the importance

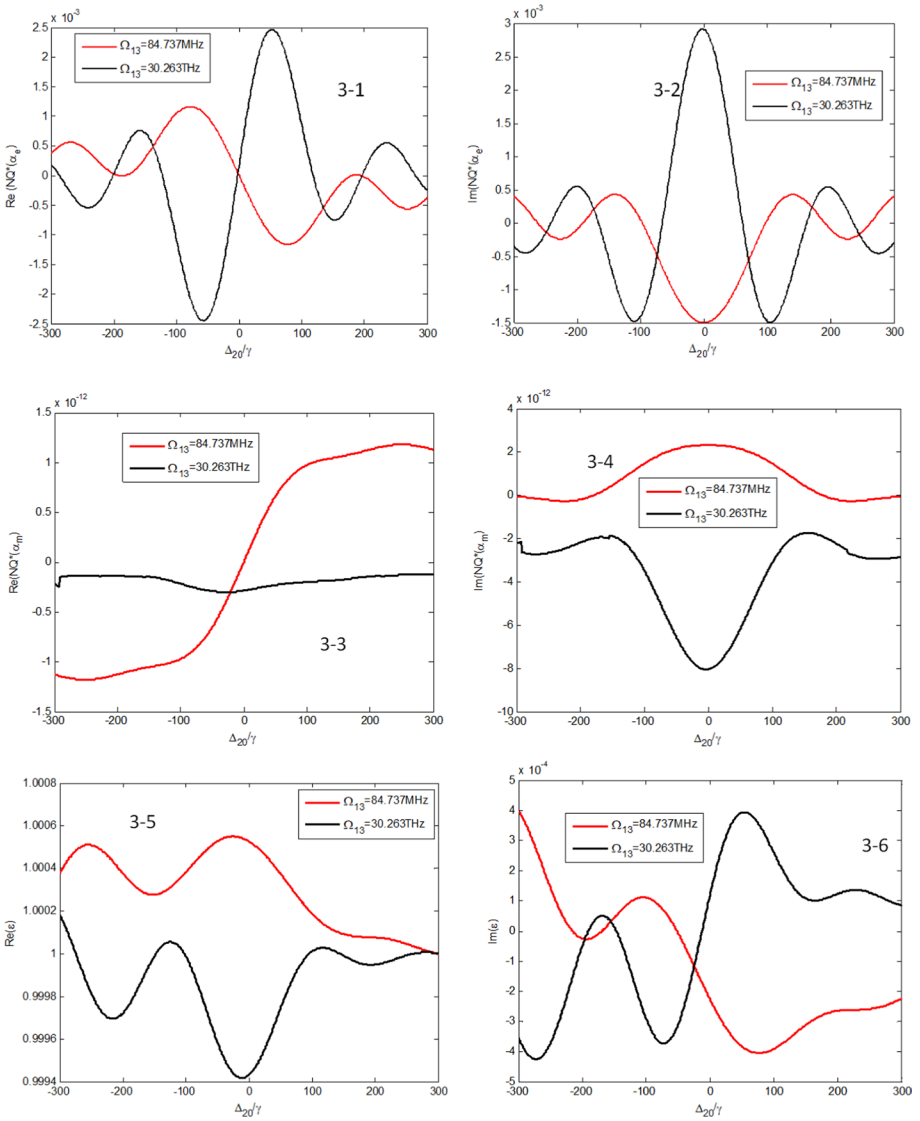

Fig. 3 Real and imaginary parts of: 3-1, 3-2 electric and 3-3, 3-4 magnetic susceptibility, 3-5, 3-6 electric and 3-7, 3-8 magnetic permeability, and 3-9 and 3-10 refractive index at the weak probe electric field $\Omega_{20} = 14.567 MHz$. Other applied fields are $\Omega_{35} = 82.901 MHz$ and $\Omega_{04} = 12.183 GHz$. (Color figure online)

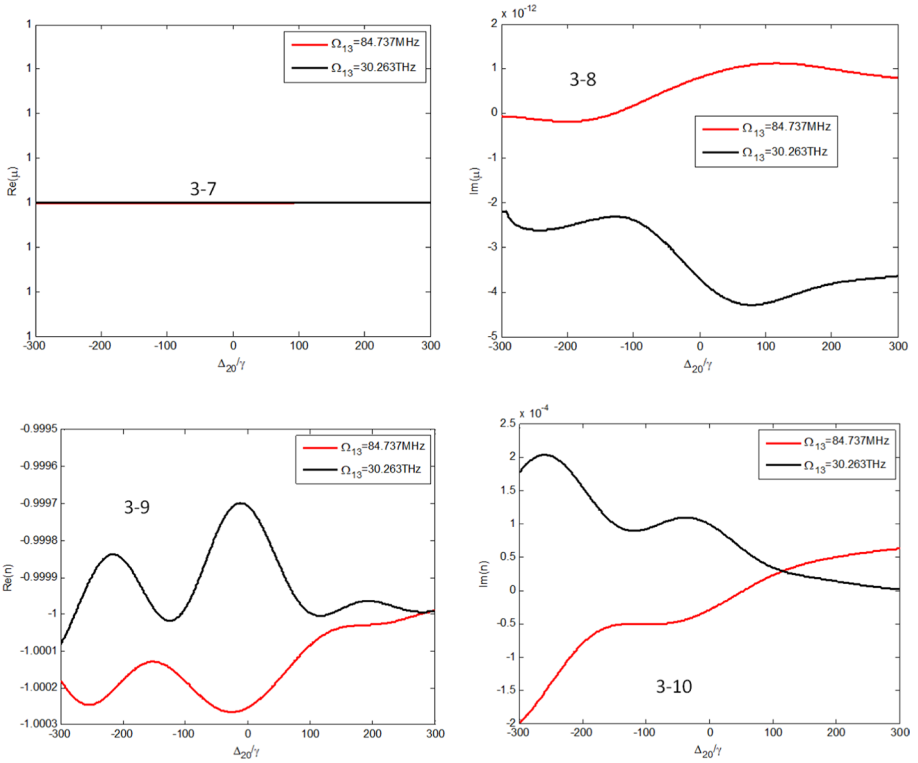

Fig. 3 (continued)

of the Ω_{25} VB WL-QD field in increasing the NRI which increased to (-2.3). There are two important things: First, the high dispersion and absorption (they are increased by more than three orders compared with Figs. 2 and 3). Second, the NRI peak occurs at the peak dispersion and zero absorption as shown in the black curve in Figs. 4-1 and 4-2. So, NRI is increased under high gain (red curve in Fig. 4-2) but the zero absorption (in the black curve, Fig. 4-2) increases NRI more.

Figure 5 shows the same set of figures at six fields, they are the pump and probe, (Ω_{20}, Ω_{13}) which are the fields applied between QD-QD states, the CB WL-QD fields (Ω_{04}, Ω_{14}), and the VB WL-QD fields (Ω_{25}, Ω_{35}). In Fig. 5-5 peak NRI corresponds to zero absorption (black curve) as shown in Fig. 5-2. Note that the value of NRI in the red

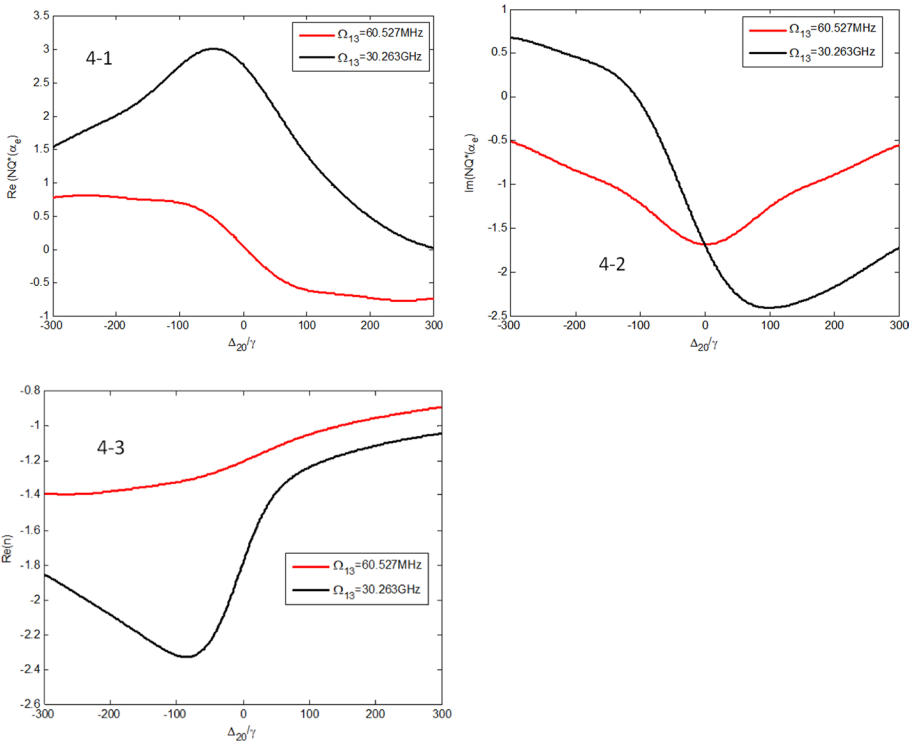

Fig. 4 Real and imaginary parts of: 4-1, 4-2 electric susceptibility. 4-3: real part of the refractive index. Applied electric fields (in addition to that appear in the inset) are $\Omega_{20} = 23.307MHz$,$\Omega_{25} = 51.630THz$, $\Omega_{04} = 32.928MHz$. (Color figure online)

curve which does not correspond to zero absorption (red curve in Fig. 5-2) has few increments from NRI in Fig. 2.

The two curves (black and red) in each of Figs. 4 and 5 can be discussed separately. The peak value of the black curves in Figs. 4-3 and 5-5 have zero absorption. In EIT one also obtains a zero absorption in the middle of the EIT bath (at the resonance frequency), thus the quantum coherence is attained at this point. For the red curve, although nether EIT, nor zero absorption but the NRI leaves the case ($NRI = -1$) that is shown in Figs. 2 and 3. This can be related to the electric and magnetic absorption and dispersion in Figs. 4 and 5 compared to those in Figs. 2 and 3 which raises the overall NRI curves. We will return to this point with Fig. 6.

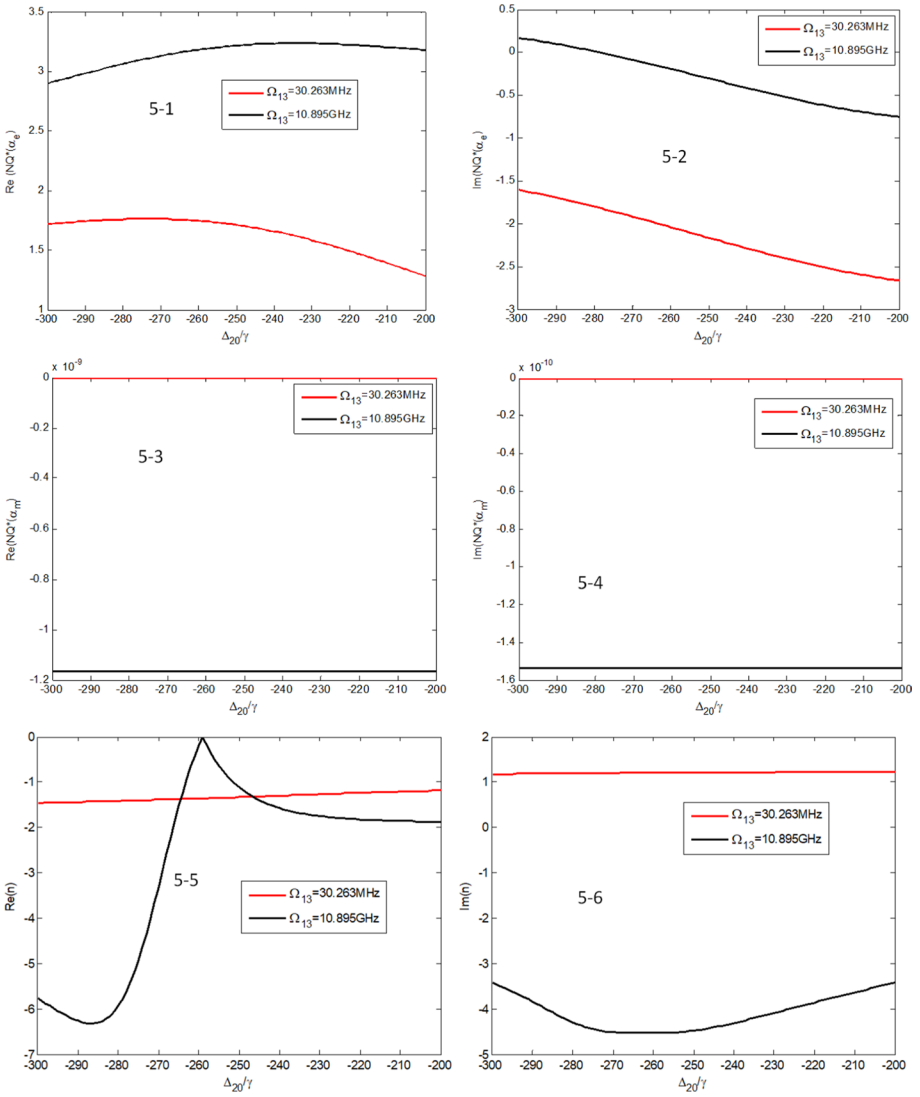

Fig. 5 Real and imaginary parts of: 5-1, 5-2 electric, and 5-3, 5-4 magnetic susceptibility, and 5-5, 5-6 refractive index. The applied electric fields are $\Omega_{14} = 15.288GHz$, $\Omega_{04} = 12.183GHz$, $\Omega_{02} = 13.110MHz$, $\Omega_{35} = 82.901MHz$, and $\Omega_{25} = 25.815GHz$. (Color figure online)

Figure 6 shows the same scenario. By reducing the CB WL-QD field (Ω_{14}) NRI is increased to (-49). The DQD system along all the detuning here is active (with a high value) for permittivity while it is passive (with a low value) for permeability (Figs. 6-5 to 6-8). From Fig. 6-6, the gain is high for a wide detuning and goes to transparency with reduced detuning. This makes the DQD have left-handed properties at the high energy side of detuning.

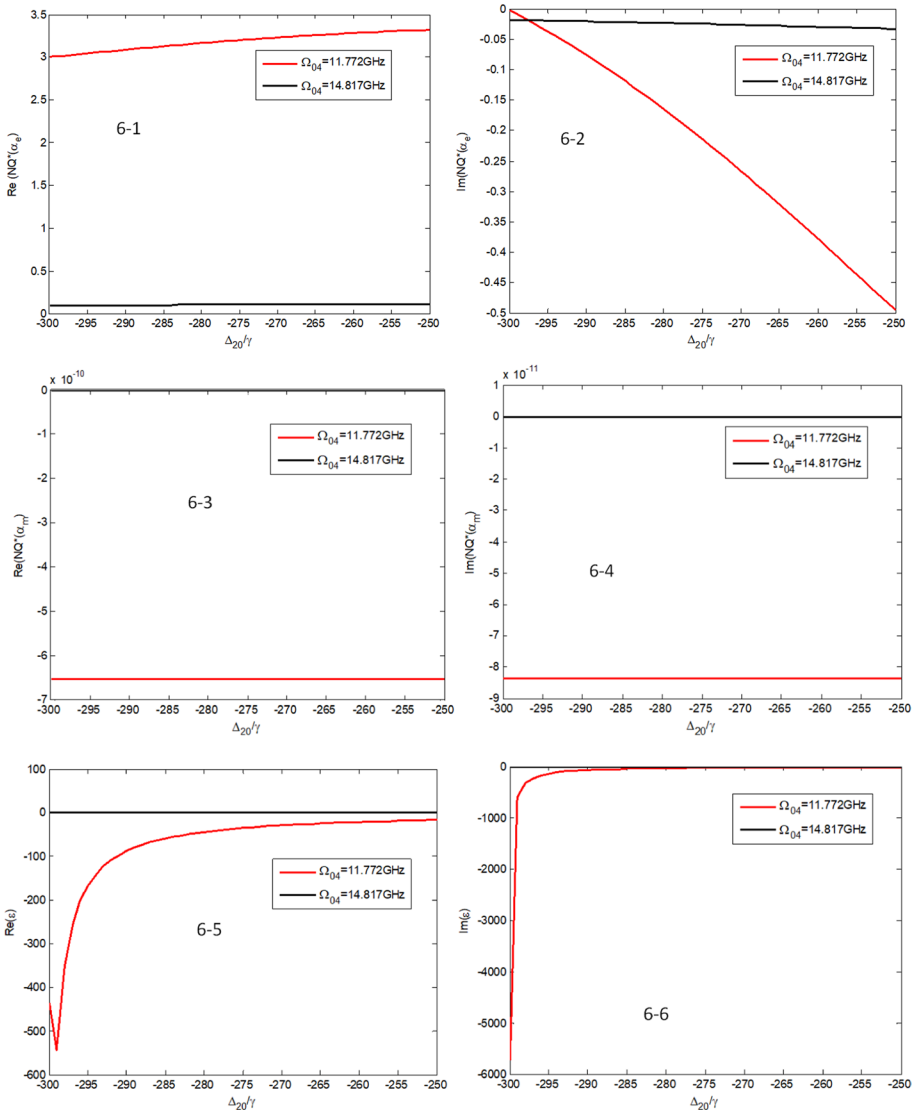

Fig. 6 Real and imaginary part of: 6-1, 6-2 electric and 6-3, 6-4 magnetic susceptibility, 6-5, 6-6 electric and 6-7, 6-8 magnetic permeability, and 6-9, 6-10 refractive index. The applied electric fields are $\Omega_{13} = 10.290GHz$,$\Omega_{25} = 25.195THz$, $\Omega_{35} = 82.901GHz$, $\Omega_{14} = 15.035GHz$, $\Omega_{02} = 12.936MHz$. (Color figure online)

Comparing Fig. 4, the black curves in Figs. 5-2, 5-4, and the red curves in Figs. 6-2, 6-4 exhibits that the main requirement in increasing NRI is the zero absorption or high electric gain connected with a low magnetic gain. For the electric gain: the black curve in Fig. 5-2 is on the same order of the red curve in Fig. 6-2, while for the magnetic gain: the red curve in Fig. 6-4 is less by one order than that of the black curve in Fig. 5-4. By checking the

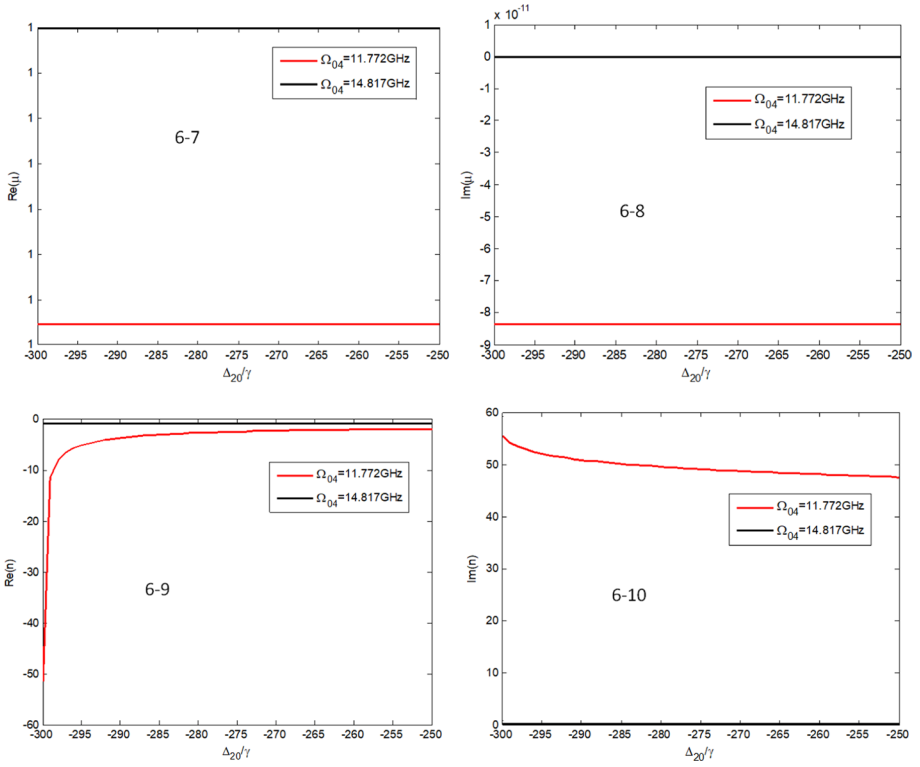

Fig. 6 (continued)

difference between the applied fields, it is shown that the high VB WL-QD electric field (Ω_{35}) is of important effect.

Fang et al. (2016) obtain more than (-5) NRI in an atomic system under single electric and magnetic fields. Wang and Zhu (2010) obtain (-15) NRI by tuning the tunneling in the QD system. The higher values obtained here show the importance of manipulation between DQD states and the effect of applying more fields. Applying more fields is known to give preferred optical properties in QD structures (Hao et al. 2012; Asadpour et al. 2011) and in atomic systems (Niu et al. 2005) where three, four, and five optical fields are examined.

Figure 7 shows a comparison between our system with other calculations which not takes the WL into account. Neglecting WL gives zero absorption but the NRI is small by ~ 16 times than that in the case of considering WL. Figure 8 shows the case of a single QD. The NRI is very small compared with the above results of the DQD system. This explains the reason for proposing the DQD system.

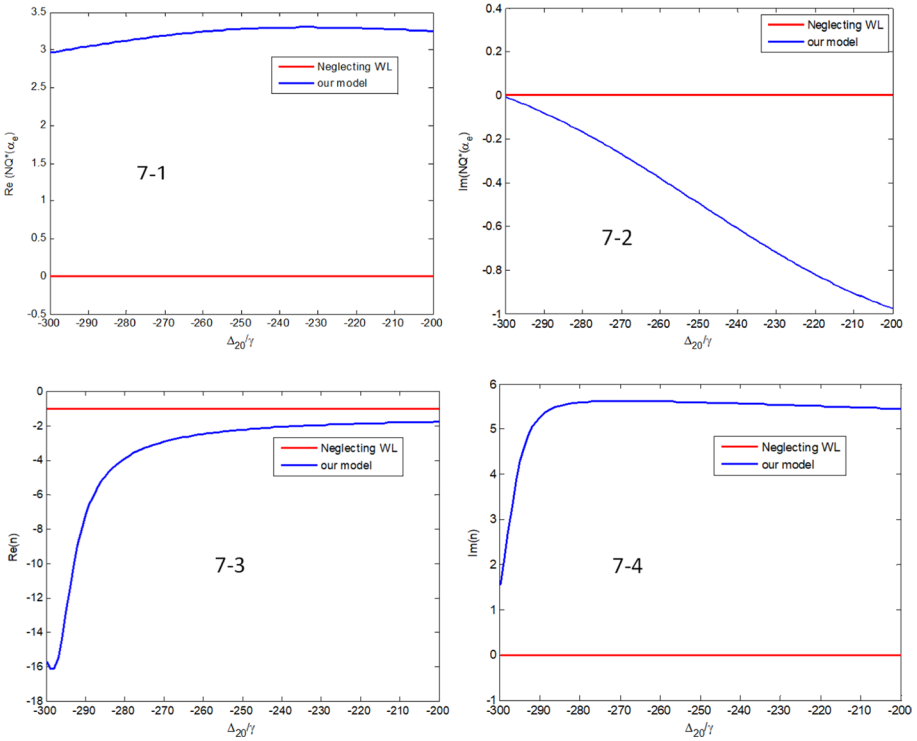

Fig. 7 Real and imaginary parts of 7-1, 7-2 electric susceptibility and 7-3, 7-4 refractive index. The applied electric fields are $\Omega_{13} = 10.290 GHz, \Omega_{13} = 10.290 GHz, \Omega_{35} = 82.901 GHz, \Omega_{25} = 25.815\, THz$, $\Omega_{04} = 11.772\, GHz, \Omega_{02} = 13.110 MHz, \Omega_{14} = 21.452\, GHz$. (Color figure online)

8 Conclusions

This work studies NRI in the DQD system considering WL under the applied electric fields: the pump, probe, and WL-QD field, in addition to the magnetic field. The dynamical equations are written by the density matrix and an orthogonalized plane wave is used between WL-QD states. The DQD system exhibit NRI ordinarily due to manipulation between states. A high NRI with neglected absorption is obtained under six fields between QD-QD, CB, and VB WL-QD fields. Higher VB WL-QD gives high NRI. It is shown that Neglecting WL reduces NRI by ~ 16 times. In single QD, the NRI is very small compared with DQD.

Compilance with ethical standards

Conflict of interest The authors declare that they have no conflict of interest.

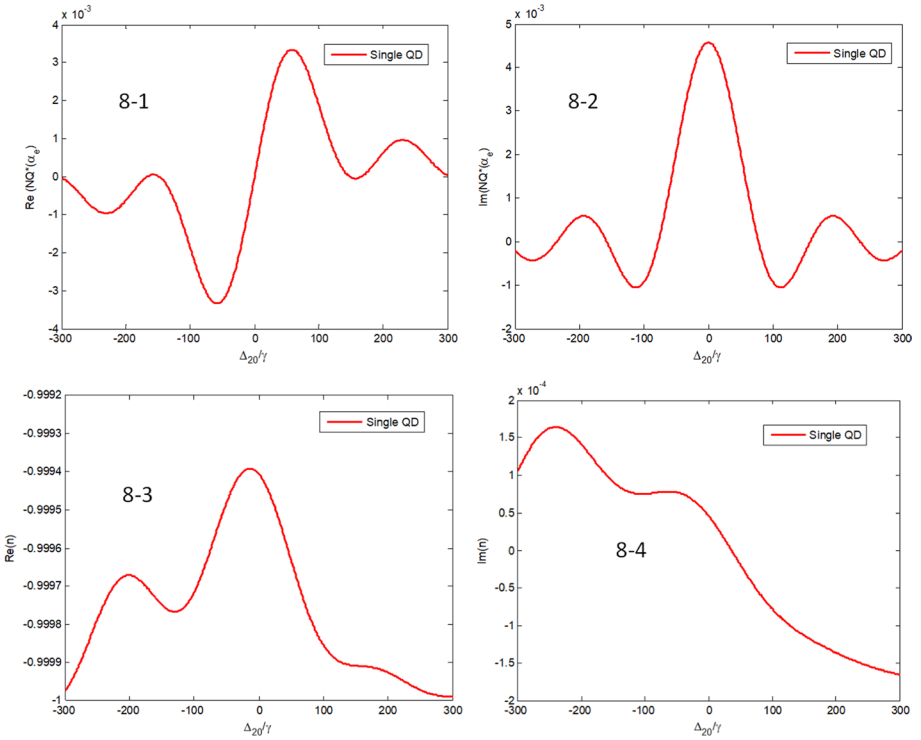

Fig. 8 Real and imaginary part of (1), (2) electric susceptibility and refractive index (3), and (4). The applied electric field is $\Omega_{02} = 13.110 MHz$. (Color figure online)

Appendix

The dynamical equations of the DQD system shown in Fig. 1 are written as,

$$\begin{aligned}\dot{\rho_{00}} = &-\gamma_0\rho_{00} + i[A_{10}(\rho_{10} - \rho_{01}) + \Omega_{20}(\rho_{20} - \rho_{02}) \\ &+ \Omega_{03}(\rho_{30} - \rho_{03}) + \Omega_{04}(\rho_{40} - \rho_{04})]\end{aligned} \tag{36-1}$$

$$\dot{\rho_{11}} = -\gamma_1\rho_{11} + i[A_{10}(\rho_{01} - \rho_{10}) + T_{21}(\rho_{21} - \rho_{11}) + \Omega_{13}(\rho_{31} - \rho_{13}) + \Omega_{14}(\rho_{41} - \rho_{14})] \tag{36-2}$$

$$\dot{\rho_{22}} = -\gamma_1\rho_{22} + i[\Omega_{20}(\rho_{02} - \rho_{20}) + T_{21}(\rho_{21} - \rho_{11}) + \Omega_{25}(\rho_{52} - \rho_{25})] \tag{36-3}$$

$$\dot{\rho_{33}} = -\gamma_{33}\rho_{33} + i[\Omega_{30}(\rho_{03} - \rho_{30}) + \Omega_{31}(\rho_{13} - \rho_{31}) + \Omega_{03}(\rho_{23} - \rho_{32}) + \Omega_{35}(\rho_{53} - \rho_{35})] \tag{36-4}$$

$$\dot{\rho_{44}} = -\gamma_4\rho_{44} + i[\Omega_{40}(\rho_{04} - \rho_{40}) + \Omega_{41}(\rho_{14} - \rho_{41})] \tag{36-5}$$

$$\dot{\rho_{55}} = -\gamma_5\rho_{55} + i[\Omega_{52}(\rho_{25} - \rho_{52}) + \Omega_{53}(\rho_{35} - \rho_{53})] \tag{36-6}$$

$$\dot{\rho_{10}} = -[(\gamma_1 + \gamma_0)\rho_{10}] + i[A_{10}(\rho_{00} - \rho_{11}) + T_{21}\rho_{20} + \Omega_{31}\rho_{30} + \Omega_{14}\rho_{40} - \Omega_{20}\rho_{12} - \Omega_{30}\rho_{13} - \Omega_{40}\rho_{14}] \tag{36-7}$$

$$\dot{\rho_{20}} = -i[(\gamma_0 + \gamma_2)\rho_{20}] + i[\Omega_{20}(\rho_{00} - \rho_{22}) + (T_{21}\rho_{10} + \Omega_{23}^{m}\rho_{30} + \Omega_{25}\rho_{25}) - (A_{10}\rho_{21} + \Omega_{30}\rho_{23} + \Omega_{25}\rho_{25})] \tag{36-8}$$

$$\dot{\rho_{30}} = -[(\gamma_0 + \gamma_3)\rho_{30}] + i[\Omega_{30}(\rho_{00} - \rho_{33}) + \Omega_{31}\rho_{10} + \Omega_{32}^{m}\rho_{20} - A_{10}\rho_{31} + \Omega_{20}\rho_{30}] \tag{36-9}$$

$$\dot{\rho_{40}} = -[(\gamma_4 + \gamma_0)\rho_{40}] + i[\Omega_{40}(\rho_{00} - \rho_{44}) + \Omega_{41}\rho_{10} + \Omega_{10}\rho_{41}] \tag{36-10}$$

$$\dot{\rho_{21}} = -[(\gamma_2 + \gamma_1)\rho_{21}] + i[T_{21}(\rho_{11} - \rho_{22}) + \Omega_{20}\rho_{01} + \Omega_{20}\rho_{31} + \Omega_{25}\rho_{51}] \tag{36-11}$$

$$\dot{\rho_{23}} = -[(\gamma_2 + \gamma_3)\rho_{23}] + i[\Omega_{23}^{m}(\rho_{33} - \rho_{22}) + \Omega_{20}\rho_{03} + T_{21}\rho_{31} + \Omega_{25}\rho_{53}] \tag{36-12}$$

$$\dot{\rho_{31}} = -[(\gamma_3 + \gamma_1)\rho_{31}] + i[\Omega_{31}(\rho_{11} - \rho_{33}) + \Omega_{30}\rho_{10} + \Omega_{23}^{m}\rho_{21} - \Omega_{10}\rho_{30} + T_{21}\rho_{23}] \tag{36-13}$$

$$\dot{\rho_{41}} = -[(\gamma_4 + \gamma_1)\rho_{41}] + i[\Omega_{41}(\rho_{11} - \rho_{44}) + \Omega_{40}\rho_{01} + Omega_{42}\rho_{21} - A_{10}\rho_{40} + T_{21}\rho_{42}] \tag{36-14}$$

$$\dot{\rho_{24}} = -[(\gamma_4 + \gamma_2)\rho_{24}] + i[\Omega_{20}\rho_{04} + T_{21}\rho_{14} - i\Omega_{04}\rho_{20} + \Omega_{14}\rho_{21} + \Omega_{52}\rho_{25}] \tag{36-15}$$

$$\dot{\rho_{25}} = -[(\gamma_2 + \gamma_5)\rho_{25}] + i[\Omega_{25}(\rho_{55} + \rho_{22}) + \Omega_{23}\rho - \Omega_{35}\rho_{23}] \tag{36-16}$$

$$\dot{\rho_{35}} = -[(\gamma_3 + \gamma_5)\rho_{35}] + i[\Omega_{23}^{m}\rho_{25} + \Omega_{35}\rho_{55} - \Omega_{25}\rho_{32}] \tag{36-17}$$

$$\dot{\rho_{43}} = -[(\gamma_4 + \gamma_3)\rho_{43}] + i[\Omega_{40}\rho_{03} + \Omega_{41}\rho_{13} - \Omega_{03}\rho_{40}\Omega_{13}\rho_{41} - \Omega_{30}\rho_{53}] \tag{36-18}$$

$$\dot{\rho_{50}} = -[(\gamma_5 + \gamma_0)\rho_{50}] + i[\Omega_{52}\rho_{20} + i\Omega_{53}\rho_{30} - \Omega_{10}\rho_{50} - \Omega_{20}\rho_{52} - \Omega_{30}\rho_{53}] \tag{36-19}$$

$$\dot{\rho_{51}} = -[(\gamma_5 + \gamma_1)\rho_{51}] + i[\Omega_{52}\rho_{20} + \Omega_{53}\rho_{30} - \Omega_{10}\rho_{50} - T_{21}\rho_{52} - \Omega_{30}\rho_{53}] \tag{36-20}$$

$$\dot{\rho_{55}} = -\gamma_5\rho_{55} + i[\Omega_{52}(\rho_{25} - \rho_{52}) + \Omega_{53}(\rho_{35} - \rho_{53})] \tag{36-21}$$

References

Abdullah, M., Noori, F.T.M., Al-Khurasan, A.H.: Terahertz emission in ladder plus Y-configurations in double quantum dot structure. Appl Opt **16**, 5186–5192 (2015)

Al-Ameri, H.H., Abdullah, M., Al-Khursan, A.H.: Entanglement in ladder-plus-Y-double quantum dot structure via entropy. Appl Opt **58**, 369–382 (2019)
Al-Husseini, H., Al-Khursan, A.H., Al-Dabagh, S.Y.: III-N QD Lasers. Open Nanosci J **3**, 1–11 (2009)
Al-Khursan, A.H., Al-Khakani, M.K., Al-Mossawi, K.H.: Third-order non-linear susceptibility in a three-level QD system. Photonics Nanostructures Fundam Appl **7**, 153–160 (2009)
Al-Khursan, A.H., Ghalib, B.A., Al-Obaidi, S.J.: A numerical simulation of optical feedback on a quantum dot lasers. Semiconductors **46**, 224–230 (2012)
Al-Nashy, B., Abdullah, M., Al-Shatravi, A.G., Al-Khursan, A.H.: Lasing without population inversion in the four-level Y-type configuration in double quantum dot system. Pramana J Phys **91**, 74 (2018)
Al-Nashy, B., Amin, S.M.M., Al-Khursan, A.H.: Kerr effect in Y- configuration double quantum dot system. J. Opt. Soc. Am. B **31**, 1991–1996 (2014)
Al-Salihi, F.R., Al-Khursan, A.H.: Electromagnetically induced grating in double quantum dot system. Opt Quantum Electron **52**, 185 (2020)
Asada, M., Atsushi, K., Suematsu, Y.: Gain and intervalence band absorption in quantum-well lasers. IEEE J. Quantum Electron **7**, 745–753 (1984)
Asadpour, S.H., Sahrai, M., Sadighi-Bonabi, R., Soltani, A., Mahrami, H.: Enhancement of Kerr nonlinearity at long wavelength in a quantum dot nanostructure. Phys E **43**, 1759–1762 (2011)
Berman, P.R.: Goos-Hänchen shift in negatively refractive media". Phys. Rev. A **6**, 067603 (2002)
Ben-Ezra, Y., Lembrikov, B.I., Haridim, M.: Acceleration of gain recovery and dynamics of electrons in QD-SOA. IEEE J. Quantum Electron **41**, 1268–1273 (2005)
Borges, H.S., Sanz, L., Villas-Boas, J.M., Neto, O.D., Alcalde, A.M.: Tunneling induced transparency and slow light in quantum dot molecules. Phys. Rev. B **85**, 115425 (2012)
Chuang, S.L.: Physics of photonic devices, 2nd edn. Wiley, New Jersy (2009)
Dolling, G., Wegener, M., Soukoulis, C.M., Linden, S.: Negative-index metamaterial at 780 nm wavelength. Opt. Lett. **1**, 53–55 (2007)
Drachev, V.P., Cai, W., Chettiar, U., Yuan, H.K., Sarychev, A.K., Kildishev, A.V., Shalaev, V.M.: Experimental verification of an optical negative-index material". Laser Phys. Lett. **1**, 49–55 (2006)
Fang, A.P., Ge, W., Wang, M., Li, F.L., Zubairy, M.S.: Negative refraction without absorption via quantum coherence. Phys. Rev. A **2**, 023822 (2016)
Foteinopoulou, S., Economou, E.N., Soukoulis, C.M.: Refraction in media with a negative refractive index. Phys. Rev. Lett. **90**, 107402 (2003)
Gorman, J., Hasko, D.G., Williams, D.A.: Charge-qubit operation of an isolated double quantum dot. Phys. Rev. Lett. **95**, 090502 (2005)
Hao, X., Wu, J., Wang, Y.: Steady-state absorption–dispersion properties and four wave mixing process in a quantum dot nanostructure. J. Opt. Soc. Am. B **29**, 420–428 (2012)
Kastel, J., Fleischhauer, M., Yelin, S.F., Walsworth, R.L.: Tunable negative refraction without absorption via electromagnetically induced chirality. Phys. Rev. Lett. **99**, 073602 (2007)
Kim, J., Chuang, S.L.: Theoretical and experimental study of optical gain, refractive index change, and linewidth enhancement factor of p-doped quantum-dot lasers. IEEE J. Quantum Electron **9**, 942–952 (2006)
Kim, J., Laemmlin, M., Meuer, C., Bimberg, D., Eisenstein, G.: Static gain saturation model of quantum-dot semiconductor optical amplifiers. IEEE J. Quantum Electron **44**, 658–666 (2008)
Lukin, M.D., Yelin, S.F., Fleischhauer, M., Scully, M.O.: Quantum interference effects induced by interacting dark resonances. Phys Rev. A **4**, 3225 (1999)
Mahmoudi, M., Sahrai, M.: Absorption-free superluminal light propagation in a quantum-dot molecule. Phys E **41**, 1772–1778 (2009)
Miladic, S., Stipsic, P., Dobardzic, E., Milivojevi, M.: Electrical control of a spin qubit in InSb nanowire quantum dots: Strongly suppressed spin relaxation in high magnetic field. Phys. Rev. B **101**, 155307 (2020)
Niu, Y., Li, R., Gong, S.: High-efficiency four-wave mixing induced by double-dark resonances in a five-level tripod system. Phys. Rev. A **71**, 043819 (2005)
Padilla, W.J., Smith, D.R., Basov, D.N.: Spectroscopy of metamaterials from infrared to optical frequencies. JOSA B **23**, 404–414 (2006)
Pendry, J.B.: Negative refraction makes a perfect lens. Phys. Rev. Lett. **18**, 3966 (2000)
Rehman, E., Al-Khursan, A.H.: All-optical processes in double quantum dot structure. Appl Opt **55**, 7337–7344 (2016)
Sahrai, M., Mehmannavaz, M.R., Sattari, H.: Optically controllable switch for light propagation based on triple coupled quantum dots. Appl Opt **53**, 2375–2383 (2014)
Shelby, R.A., Smith, D.R., Schultz, S.: Experimental verification of a negative index of refraction. Science **5514**, 77–79 (2001)

Smith, D.R., Smith, D.R., Padilla, W.J., Vier, D.C., Nemat-Nasser, S.C., Schultz, S.: Composite medium with simultaneously negative permeability and permittivity. Phys. Rev. Lett. **18**, 4184 (2000)
Stavrou, V.N.: Spin qubits: spin relaxation in coupled quantum dots. J. Phys. Condens. Matter **30**, 455301 (2018)
Tarasov, G.G., Zhuchenko, Y.Z., Lisitsa, M.P., Mazur, Y.I., Wang, Z.M., Salamo, G.J., Warming, T., Bimberg, D., Kissel, H.: Optical detection of asymmetric quantum-dot molecules in double-layer InAs/GaAs structures. Semiconductors **40**, 79–83 (2006)
Verhagen, E., Waele, R., Kuipers, L., Polman, A.: Three-dimensional negative index of refraction at optical frequencies by coupling plasmonic waveguides. Phys. Rev. Lett. **105**, 223901 (2010)
Veselago, V.G.: The electrodynamics of substances with simultaneously negative values of ε and μ. Phys-Uspekhi **10**, 509–514 (1968)
Veselago, V., Braginsky, L., Shklover, V., Hafner, C.: Negative refractive index materials. J. Comput Theor Nanosci **2**, 189–218 (2006)
Veselago, V.G., Narimanov, E.E.: The left hand of brightness: past, present and future of negative index materials. Nat. Mater. **10**, 759–762 (2006)
Villas-Bôas, J.M., Govorov, A.O., Ulloa, S.E.: Coherent control of tunneling in a quantum dot molecule. Phys. Rev. B **69**, 125342 (2004)
Wang, H., Zhu, K.: Voltage-controlled negative refractive index in vertically coupled quantum dot systems. Optics Communications **283**, 4008–4011 (2010)
Wang, L., Guo, G., Wei, D., Cao, G., Tu, T., Xiao, M., Guo, G.: Gates controlled parallel-coupled double quantum dot on both single layer and bilayer graphene. Appl. Phys. Lett. **99**, 112117 (2011)
Zhao, S.C., Qian, X.F., Zhang, Y.P., Zhang, Y.A.: Negative refraction with little loss manipulated by the voltage and pulsed laser in double quantum dots. Prog Theor. Phys. **2**, 243–250 (2012)